NON-PEER-REVIEWED PREPRINT

Submitted to EarthArXiv

Mutual interactions between aquifer thermal energy storage and groundwater extraction: global sensitivity insights

Zerui Mi[a*], Luka Tas[a], Wouter Deleersnyder[a,b,c], Thomas Hermans[a]

a Department of Geology, Ghent University, Ghent, Belgium
b University of British Columbia, Department of Earth, Ocean and Atmospheric Sciences, Vancouver, British Columbia, Canada
c KU Leuven, Department of Physics, Kortrijk, Belgium
* Corresponding author: Zerui Mi, Mia.mi@ugent.be

This manuscript is a non-peer-reviewed preprint submitted to EarthArXiv
February 2026

Mutual interactions between aquifer thermal energy storage and groundwater extraction: global sensitivity insights

Zerui Mi[a*], Luka Tas[a], Wouter Deleersnyder[a,b,c], Thomas Hermans[a]

a Department of Geology, Ghent University, Ghent, Belgium
b University of British Columbia, Department of Earth, Ocean and Atmospheric Sciences, Vancouver, British Columbia, Canada
c KU Leuven, Department of Physics, Kortrijk, Belgium
* Corresponding author: Zerui Mi, Mia.mi@ugent.be

Abstract: Aquifer Thermal Energy Storage (ATES) is increasingly deployed in groundwater protection zones, motivating a quantitative assessment of thermal impacts on public-supply wells and the influence of supply-well pumping on ATES performance. In the Campine Basin (Belgium), we simulate three settings: balanced operation, seasonal imbalance, and multi-system deployment. Using a groundwater flow and heat-transport model. Uncertainty in hydrogeological properties and operational settings is represented with Latin Hypercube sampling, and distance-based Generalized Sensitivity Analysis (DGSA) ranks parameter sensitivity for both supply-well temperature disturbance (ΔT_{supply}) and ATES recovery efficiency. Supply-well ΔT_{supply} decreases with distance but can exceed natural seasonal variability at close spacing, particularly under imbalance and dense layouts. In the near field (≤75 m), range ΔT_{supply} is mainly controlled by ATES throughput and seasonal imbalance under pumping-induced convection from ATES cycling superimposed on continuous supply-well abstraction. At larger distances (≥200 m), variability is governed primarily by conductivity contrasts, porosity, and dispersivity, together with regional flow and the supply-well induced hydraulic gradient. Strong background flow and short spacing reduce recovery efficiency, and multi-system cases show cumulative plume interference. For the Campine Basin and similar hydrogeological settings, the results support site-specific setback design, operational constraints, and monitoring requirements, and the same workflow can be applied to other aquifers to derive locally appropriate permitting guidance.

Keywords: Aquifer Thermal Energy Storage (ATES); groundwater protection; thermal recovery efficiency; sensitivity analysis

1. Introduction

With the accelerating push toward global carbon neutrality, there is a growing demand for low-carbon heating and cooling technologies (Mahon et al., 2022). Aquifer Thermal Energy Storage (ATES) is such an emerging subsurface renewable energy solution. It operates through seasonally storing excess heat and cold in groundwater from aquifers and recovering it when needed. An ATES system typically consists of one or multiple well doublets (composed of one warm and one cold well) (Bloemendal et al., 2018; Hähnlein et al., 2013). By utilizing the high thermal capacity and natural insulation of aquifers, ATES enables efficient underground storage and recovery of thermal energy (Brielmann et al., 2009; Stemmle et al., 2025). Today, around 3500 ATES systems are installed worldwide, especially in the Netherlands, where they play an increasingly important role in urban decarbonization strategies (Jackson et al., 2024; Stemmle et al., 2025).

However, with large-scale deployment, the subsurface may become crowded and may potentially be developed in close proximity to drinking water abstraction wells and their protection zones (Bonte, Stuyfzand, van den Berg, et al., 2011a; Possemiers et al., 2014). This siting trend has raised concerns over potential thermal disturbances to the groundwater environment. The alternating heat and cold injections produce thermal plumes that alter the natural temperature field, particularly under unbalanced or long-term operation (Hähnlein et al., 2013; Pophillat et al., 2020). These temperature anomalies may affect not only the physical properties of groundwater but also trigger a series of chemical and biological reactions (Allen, 1983; Blum et al., 2021; Bonte, Stuyfzand, van den Berg, et al., 2011b; Griebler et al., 2016). As such, concerns are raised about the effect of ATES on drinking water production.

From a policy perspective, the EU Water Framework Directive (WFD) defines "pollution" to include the introduction of heat into water bodies, but does not specify any numerical temperature rise or distance indicators (EU-WFD, 2000). Many countries have independently set limits based on their own ecological and water resource management needs. For example, Switzerland allows groundwater temperatures to be within ±3 K, and France limits interannual temperature differences to within ±11 K (Haehnlein et al., 2010). By contrast, Belgium has no nationwide ATES-specific ΔT cap on groundwater. In Flanders, open-loop ATES is regulated via the general environmental permit within the VLAREM framework, which caps reinjection temperature at 25 °C and generally excludes installations in wellhead protection Zones I–II where works deeper than 2.5 m are prohibited unless required for public water supply, while projects in Zone III are assessed case by case (VLAREM II, 2024). Overall, this precautionary, permit-based regime, in the absence of a ΔT-based standard, constrains ATES deployment within Flemish groundwater protection zones.

To characterize how ATES operation perturbs groundwater systems, numerous case and review studies have combined long-term monitoring with three-dimensional flow and heat-transport modelling. For individual systems in the Netherlands and Belgium, these studies delineate the spatial extent and persistence of warm and cold plumes and show that

stratigraphy and confining layers exert a strong control on vertical heat migration (Possemiers et al., 2014; Visser et al., 2015). Several investigations further demonstrate that ATES-induced temperature changes can modify carbonate equilibria, mobilize redox-sensitive species and alter microbiological communities, including in settings where groundwater is abstracted for drinking-water supply, although observed changes in groundwater quality have generally remained within drinking-water standards where setback distances are sufficiently large (Bonte, Stuyfzand, van den Berg, et al., 2011a; Possemiers et al., 2014). Building on this process understanding, analytical and numerical frameworks have been developed to predict thermal plume evolution and thermal interference between neighbouring systems, and to quantify temperature changes at compliance points in the aquifer (Pophillat et al., 2020; Tas et al., 2025). At larger spatial scales, planning and site-suitability studies map the technical potential of ATES and delineate where deployments are compatible with water-resource protection objectives, explicitly considering sensitive receptors such as drinking-water well fields and protection zones, contaminated sites and groundwater-dependent ecosystems (Bloemendal et al., 2018; Borko et al., 2025; Stemmle et al., 2022). However, despite this growing body of work on ATES-induced temperature changes in aquifers, systematic, site-specific assessments of thermal perturbations at drinking-water abstraction wells within groundwater-protection zones remain scarce.

Most of these studies, however, adopt a one-way perspective in which ATES perturbs groundwater conditions, while the influence of drinking-water abstraction on ATES behavior is not explicitly considered. In reality, the interaction between ATES systems and public-supply wells is inherently bidirectional. Pumping wells modify hydraulic gradients and streamline patterns, potentially accelerating advective heat transport and shortening thermal residence times, thereby reducing the thermal recovery efficiency of nearby ATES systems (Bloemendal & Hartog, 2018; Tas et al., 2025). In dense well fields or regulated protection zones, this feedback may both constrain the viable operating window of ATES and increase the risk of thermal disturbances at drinking-water wells, effectively limiting the capacity of aquifers to accommodate both renewable-energy use and drinking-water abstraction. Yet, quantitative evaluations of this reciprocal influence, particularly under the regulatory constraints and safety margins that apply in groundwater-protection zones, remain limited.

This study addresses these gaps by analyzing the coupled interaction between an ATES system and a groundwater protection zone in the Campine Basin region of Belgium. We consider three representative operating scenarios: (i) balanced injection-extraction operation, (ii) seasonally imbalanced operation, and (iii) multiple ATES systems under imbalanced conditions. A three-dimensional groundwater-flow and heat-transport model is used to simulate thermal plume evolution and temperature changes at a representative drinking-water well. Uncertainty in key aquifer parameters, including porosity, permeability and thermal properties, is incorporated through Monte Carlo sampling. Distance-based Generalized Sensitivity Analysis (DGSA) is then applied to systematically evaluate the relative importance of subsurface properties and ATES-well separation for three response metrics: the peak summer temperature and the seasonal temperature range at the abstraction well, the

thermal recovery efficiency of the ATES system. Taken together, our analyses demonstrate how site-specific numerical modelling combined with global sensitivity analysis can be used to jointly appraise drinking-water well temperature impacts and ATES performance. This study provides a generally applicable way to analyse ATES-well interactions under uncertainty and supports the design and evaluation of ATES deployment.

2. Materials and methods

2.1. Study area

The Campine Basin in northeastern Flanders, Belgium, is a major groundwater resource region, where about 50% of the drinking water supply is abstracted from the Berchem/Voort Sands and Diest Sands aquifers (VMW, 2020). These homogeneous sandy units provide both a secure source of drinking water and favorable conditions for ATES, as their relatively high transmissivity allows the required pumping rates, while the gentle regional hydraulic gradient results in relatively slow natural groundwater flow velocities that limit advective heat losses (Bloemendal & Olsthoorn, 2018; Lee, 2010). The Berchem/Voort Sands constitute the main public-supply aquifer in the area. The overlying Diest Sands act as a secondary aquifer with moderate permeability, while the underlying Boom Clay aquitard serves as an effective hydraulic barrier, minimizing vertical exchange with deeper systems.

The basin is characterized by a temperate climate with annual recharge of approximately 240-310 mm (Vandersteen & Gedeon, 2012). Groundwater flow is mainly driven by precipitation recharge and gentle topography, producing predominantly east-west hydraulic gradients on the order of 3×10^{-4} that are relatively stable over multi-year periods, with superimposed seasonal fluctuations (Casillas-Trasvina et al., 2024), although seasonal fluctuations occur.

The area is subject to strict groundwater protection under EU and Flemish legislation (European Commission, 2006; Flemish Government, 1984). Three concentric zones are defined around drinking water wells based on groundwater travel times: a 24-h capture zone (<50 m), a 60-day travel-time zone (≈300 m), and a broader recharge area (≈2 km) (= simplified). This coexistence of regulated abstraction protection zones and high ATES potential makes the Campine Basin an ideal case study for evaluating not only how ATES operations may affect groundwater resources, but also how abstraction wells can, in turn, influence ATES performance. The study area comprises the protection zones around a drinking-water well field in the Campine Basin (Figure 1). This well field was selected because its abstraction regime and protection zoning are typical of many drinking-water abstractions in the basin, so that the interactions analyzed here are relevant beyond this specific location.

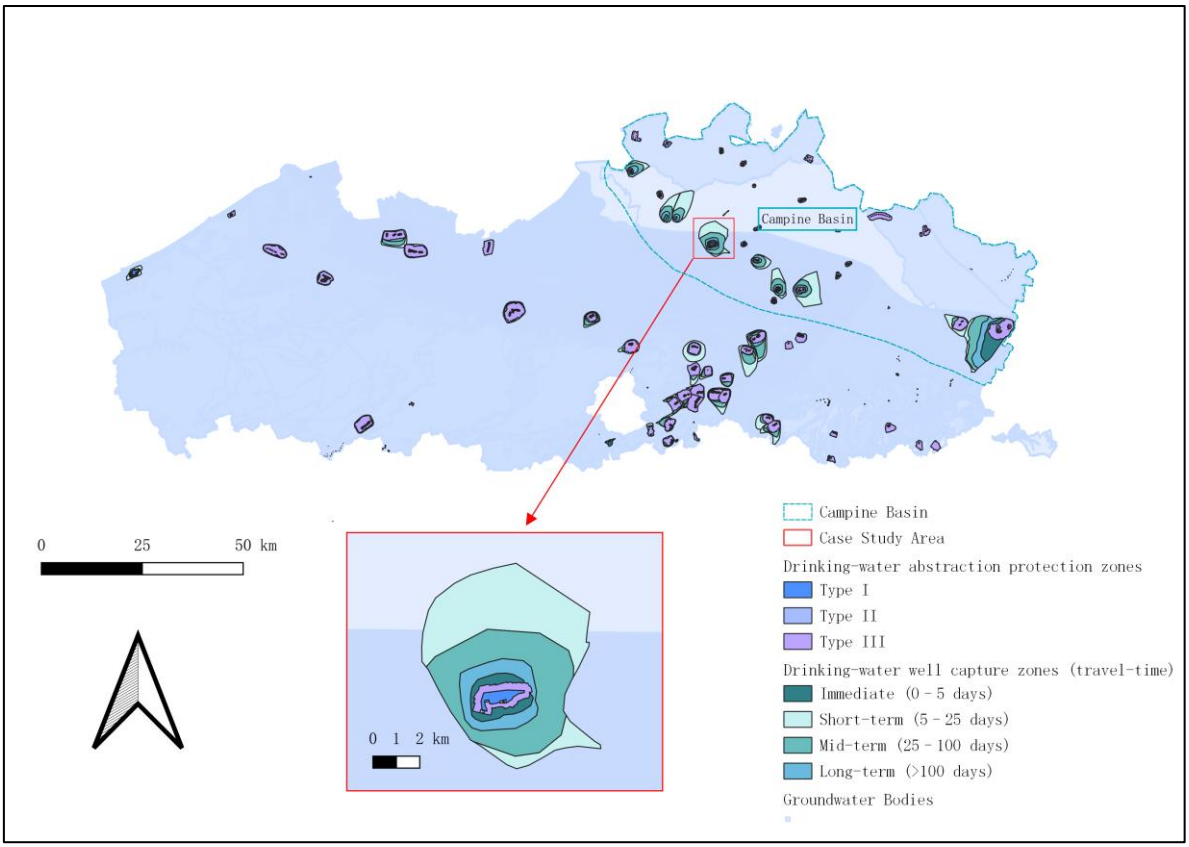

Figure 1: Case Study Area and Groundwater Protection Zones in the Campine Basin

2.2. Governing equations

Groundwater flow was described by the three-dimensional transient groundwater flow equation used in the MODFLOW 6 Groundwater Flow (GWF) model (Langevin et al., 2017):

$$\frac{\partial}{\partial x}\left(K_x \frac{\partial h}{\partial x}\right) + \frac{\partial}{\partial y}\left(K_y \frac{\partial h}{\partial y}\right) + \frac{\partial}{\partial z}\left(K_z \frac{\partial h}{\partial z}\right) - Q_w = S \frac{\partial h}{\partial t} \quad (1)$$

where h $[m]$is hydraulic head, K_x, K_y, K_z[m s^{-1}] are hydraulic conductivities in the x, y, and z direction respectively, Q_w[s^{-1}] is the volumetric source-sink term per unit aquifer volume, S[m^{-1}] is the specific storage and t[s] is time.

Heat transport was represented by the advection-dispersion-conduction equation, in which temperature was treated analogously to a conservative solute in the MODFLOW 6 Groundwater Transport (GWT) formulation (Hecht-Méndez et al., 2009; Langevin et al., 2022; Tas et al., 2025):

$$(\varphi \rho_w c_w + (1-\varphi)\rho_s c_s)\frac{\partial T}{\partial t} = \nabla \cdot (\lambda_{\text{eff}} \nabla T) - \nabla \cdot (\rho_w c_w \, qT) + Q_T \quad (2)$$

Where T [°C] is groundwater temperature, φ[-]is porosity, ρ_w and ρ_s [kg m^{-3}] and c_w and c_s [J kg^{-1} K^{-1}] are the densities and specific heat capacities of water and the solid matrix,

185 respectively, so that $\rho_w c_w$ and $\rho_s c_s$ are the corresponding volumetric heat capacities[J m^{-3} K^{-1}]. The effective thermal conductivity of the saturated porous medium is given by

187 $$\lambda_{\text{eff}} = \varphi k_{wf} + (1 - \varphi) k_{ws}$$

188 where k_{wf} and k_{ws} [W m^{-1} K^{-1}] are the thermal conductivities of groundwater and the
189 solid matrix. q [m s^{-1}] is the Darcy flux vector obtained from the flow solution as $q =$
190 $-\mathbf{K}\nabla h$, and Q_T [W m^{-3}] represents external heat sources or sinks associated with injection
191 of warm or cold water. This one-way coupling approach assumes that the imposed
192 temperature variations (±5 °C) do not affect groundwater density or viscosity and therefore
193 do not feed back on the flow field (Hecht-Méndez et al., 2009; Ma & Zheng, 2010).

194 In addition to groundwater temperature perturbations, system performance was quantified
195 through the seasonal thermal recovery efficiency of ATES operation (Sommer et al., 2015;
196 Tas et al., 2025):

$$\eta = \frac{\int_{t_0}^{t_1} Q_{\text{out}}(t)[T_{\text{out}}(t) - T_0]\ dt}{\int_{t_0}^{t_1} Q_{\text{in}}(t)[T_{\text{in}}(t) - T_0]\ dt} \quad (3)$$

197 where $Q_{\text{in}}(t)$and $Q_{\text{out}}(t)$[m³ s^{-1}] are the time-dependent injection and abstraction rates of
198 the ATES wells, $T_{\text{in}}(t)$and $T_{\text{out}}(t)$[°C] are the corresponding injection and abstraction
199 temperatures, T_0[°C] is the undisturbed groundwater temperature, and $t_0$and $t_1$denote the
200 start and end of one storage–recovery cycle.

201 *2.3. Numerical modeling framework*

202 A three-dimensional groundwater flow and heat transport model was implemented in
203 MODFLOW 6 (Langevin et al., 2017, 2022) using the GWF and GWT packages. Model pre-
204 and post-processing were conducted in ModelMuse (Winston, 2009), and batch simulations
205 were managed with FloPy (Bakker et al., 2016).

206 The model domain covered 9 × 9 km horizontally and 95 m vertically, encompassing the
207 public supply wells and their associated protection zones. The subsurface was represented by
208 six hydrostratigraphic layers (Casillas-Trasvina et al., 2022a; Databank Ondergrond
209 Vlaanderen, n.d.): cover sands, Pleistocene-Pliocene sands, a Pliocene clay aquitard, Diest
210 Sands, Berchem/Voort Sands, and the underlying Boom Clay. Of these, Berchem/Voort is
211 the target aquifers for this study, while the upper part of the Boom Clay was included mainly
212 for its confining and thermal buffering properties. All layers were assumed horizontally
213 homogeneous and isotropic, with vertical anisotropy represented by $K_z = 0.1K_x$. The cover
214 sands were modeled as unconfined, and the deeper units as confined.

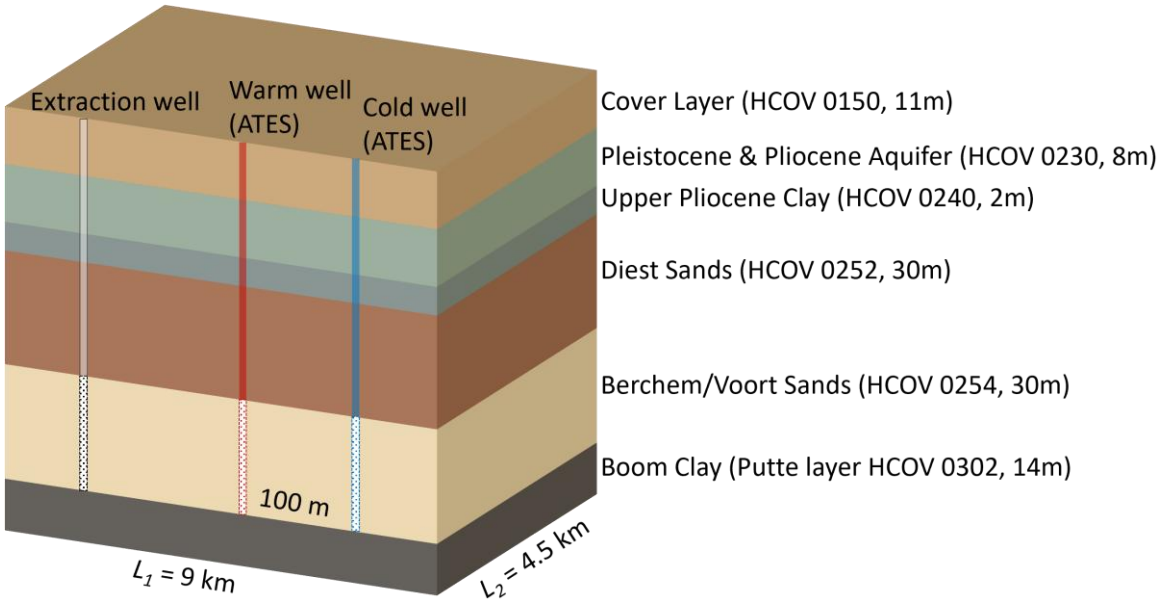

Figure 2： Schematic representation of the model domain including a public-supply extraction well and an ATES doublet.

An unstructured DISV grid with quadtree refinement was used. Six refinement levels were applied, each halving cell width, resulting in cell sizes from about 5 m around the pumping and ATES wells to about 300 m towards the model boundaries. Tests with alternative refinement patterns indicated that this level of local refinement was the coarsest that eliminated grid-related artefacts in the near-well hydraulic and thermal plumes, whereas finer grids only marginally changed plume dimensions but substantially increased computational cost. Vertically, the model honored the six hydrostratigraphic units. To better resolve vertical hydraulic and thermal gradients in the main production and ATES aquifers, the fourth unit (Diest Sands) was subdivided into three numerical layers and the fifth unit (Berchem/Voort Sands) into six, while the remaining units were represented by a single layer each, giving a total of 12 computational layers. This refinement yields individual layer thicknesses on the order of several meters within the production and ATES intervals, which is sufficient to capture the relevant vertical gradients at the scale of interest while keeping computational effort manageable. An initial steady-state stress period was used to establish starting conditions. The subsequent transient simulation covered five annual cycles represented by ten six-month stress periods, with adaptive time stepping using a maximum first time-step of 5 days in the first transient period and 10 days thereafter and a time-step multiplier of 1.5. Model outputs at the public-supply well were stored at each transient time step, resulting in 63 temperature samples over the 5-year simulation (approximately monthly resolution), which were used as the input time series for the DGSA.

Boundary conditions were defined consistently for flow and heat. Constant-head boundaries on the east and west were specified to reproduce the regional natural hydraulic gradient, which is of order 10^{-4} m m^{-1} and consistent with the regional-scale model (Casillas-Trasvina et al., 2022b), while the north, south, and bottom were no-flow. A uniform recharge rate of 315 mm yr^{-1} was applied at the surface, entering the aquifer at the background temperature

of 10 °C. No-flow and bottom boundaries were treated as adiabatic. Initial conditions were a uniform hydraulic head of 11 m, expressed as meters above sea level (m a.s.l.), and a uniform temperature of 10 °C. No-flow and bottom boundaries were treated as adiabatic. For ATES operation, injection wells prescribed constant water temperatures during operation (15 °C injection in the warm well in summer and 5 °C in the cold well in winter), while the corresponding ATES abstraction wells returned water at model-calculated outlet temperatures, computed as the average temperature of all model layers intersecting the well screen. The well spacing of the ATES doublet is 100 m, as it was confirmed that this does not cause thermal breakthrough for the considered scenarios. Public-supply abstraction was modeled as a single equivalent extraction well in the Berchem/Voort Sands.

Hydraulic and thermal parameters were assigned from regional datasets (Vandersteen et al., 2014) and recent stochastic studies in the same aquifer (Casillas-Trasvina et al., 2022a, 2024; Tas et al., 2025). Table 1 provides a summary of all parameter values and the ranges used in sensitivity analysis.

Table 1: Parameter values and ranges used in the numerical modeling and sensitivity analysis (adapted from Vandersteen et al., 2014; Casillas-Trasvina et al., 2024; Tas et al., 2025, and this study).

	Unit	Value / Range	Note
Hydrogeological			
kx_0150	m/s	3.08×10^{-3}	hydraulic conductivity of Cover sands
kx_0230	m/s	2.51×10^{-4}	Plio-Pleistocene sands
kx_0240	m/s	4.50×10^{-6}	Pliocene clay aquitard
kx_0252	m/s	1.2×10^{-5} - 6×10^{-4}	Diest Sands
kx_0254	m/s	2.3×10^{-7} - 2×10^{-4}	Berchem/Voort Sands
kx_0302	m/s	1.25×10^{-11}	Boom Clay
φ_0252	-	0.20 - 0.40	Porosity of Diest Sands
φ_0254	-	0.25 - 0.45	Porosity of Berchem/Voort Sands
φ_eff	-	0.60 - 0.95	Effective porosity
grad	m/m	-7×10^{-4} - -1×10^{-4}	Regional gradient
Thermal			
k_f	W/m·K	0.55 - 0.65	Thermal conductivity (fluid)
k_s	W/m·K	2 - 4	Thermal conductivity (solid)
a_l	m	1 - 8	Longitudinal dispersivity
a_T	m	0.1 - 1.0	Transverse dispersivity (~0.1 a_l)
c_f	J/kg·K	4140	Heat capacity (fluid)
c_s	J/kg·K	800	Heat capacity (solid)
ρ_f	kg/m³	1000	Fluid density
ρ_s	kg/m³	2690	Rock density
Operational			

Q_in/ex	m³/h	80 - 120	ATES injection/extraction
Q_pump	m³/d	-22,000	Public-supply extraction well
spacing	m	100	ATES warm–cold well spacing
angle	°	0 - 360	ATES orientation
R	m	75 - 500	ATES-well distance
imbalance_Q	-	1 - 1.5	Seasonal imbalance factor
T_inj	°C	15 (warm well, summer); 5 (cold well, winter)	Injection temperature
T_bg	°C	10	Background groundwater temperature

2.4. Scenario design

Three representative scenarios were defined to evaluate ATES impacts under typical operating conditions in the Campine Basin. The first scenario represents a single balanced system, with equal seasonal injection and extraction volumes (80-120 m³/h) and prescribed temperatures of 15 °C in summer and 5 °C in winter. The second scenario considers a single imbalanced system, where the summer injection flow is increased (imbalance ratio up to 1.5) to mimic larger cooling demand. The third scenario simulates a multi-system imbalanced case, with multiple ATES doublets arranged in checkerboard and lane patterns at a short distance (75 m) from the pumping well to represent dense urban deployment.

For each scenario, the distance R between the center of the ATES doublet and the public-supply well was used as a control parameter. In the balanced reference case R was set to 75, 200 and 500 m, in the imbalanced single-system case R was densely sampled between 175 and 300 m, and in the multi-system case R was fixed at 75 m to represent dense urban deployment. Model outputs focused on groundwater temperature responses at the pumping well (time series, maximum temperature difference) and ATES performance (thermal recovery efficiency). These complementary indicators provide the basis for evaluating both the potential risk to the water supply and the feedback of pumping conditions on ATES efficiency.

2.5. DGSA framework

Distance-based Generalized Sensitivity Analysis (DGSA) was employed to quantify the importance of uncertain parameters on ATES-induced groundwater responses (Park et al., 2016). For each combination of operating scenario and ATES-well distance, 500 parameter realizations were generated using Monte Carlo simulation combined with Latin Hypercube Sampling (Baalousha, 2016; Zhang & Pinder, 2003), and the coupled flow–heat model was run for each realization under the three representative operating scenarios. The simulated temperature time series at the public-supply extraction well and the thermal recovery efficiency were used as input for the DGSA.

In DGSA, the ensemble of model outputs is first partitioned into a small number of classes with similar temporal behavior. In this study, pairwise Euclidean distances between the 5-year temperature trajectories at the public-supply extraction well were computed, and a

distance-based K-medoids clustering was applied to separate the simulations into two distinct response groups with clearly different patterns of thermal impact at the well. For each uncertain parameter, DGSA then compares the empirical cumulative distribution of its sampled values within each response group with the global distribution over all realizations. Parameters for which the conditional distributions associated with the response groups deviate strongly from the global distribution are interpreted as influential, because they discriminate between the two types of model response (Park et al., 2016; Perzan et al., 2021; Scheidt et al., 2018).

Parameter interaction effects were analyzed using the conditional formulation of DGSA, in which the range of a conditioning parameter is partitioned into value intervals and the DGSA sensitivity of a second parameter is recomputed within each interval; systematic changes in sensitivity across intervals are taken as evidence of interaction between the two parameters (Park et al., 2016; Scheidt et al., 2018). All first-order and interaction indices were obtained with the open-source pyDGSA package for Python, which implements this DGSA framework (Perzan et al., 2021).

2.6. Thermal impact on the public-supply well and ATES efficiency criteria

The thermal impact of ATES at the public-supply well was evaluated using the maximum seasonal temperature range ΔT. For each realisation, ΔT was defined as the difference between the highest and lowest simulated water temperature at the extraction well over the 5-year simulation period, which in all cases occurred between a late-summer maximum and a winter minimum. This measure reflects the seasonal temperature range at the pumping well. Under natural conditions in temperate aquifers at 15-20 m depth, this range typically does not exceed about 0.5 °C (Anderson, 2005). Hydrochemical studies on ATES and related shallow-geothermal systems indicate that groundwater quality is relatively insensitive to small temperature perturbations: changes in groundwater temperature of a few degrees around ambient conditions do not produce systematic shifts in major-ion chemistry or trace metals (Bonte, 2013; Possemiers et al., 2014). Using the maximum seasonal temperature range ΔT as a metric has two advantages: it summarises the full temperature time series at the well into a single value that represents the seasonal variation in groundwater temperature, and it can be directly compared with the natural seasonal range reported for similar aquifers (Anderson, 2005*)*. Because the well supplies drinking water, a conservative threshold of $\Delta T \leq 0.5$ °C is adopted here, which is substantially smaller than the temperature changes over which previous hydrochemical studies have observed negligible effects on groundwater quality.

In addition, performance was evaluated in terms of recovery efficiency. Previous analytical and numerical studies, as well as evaluations of operating ATES systems, have shown that recovery efficiency is strongly controlled by the balance between advective displacement losses and conductive–dispersive heat losses (Bloemendal & Hartog, 2018). When regional groundwater flow is relatively strong compared with the spatial extent of the thermal plume, advective displacement dominates and recovery efficiency declines rapidly, whereas in weak-flow settings the stored heat remains largely within the thermal radius and efficiency

instead decreases with increasing surface-area-to-volume ratio of the stored volume (A/V) *(Bloemendal & Hartog, 2018; Tas et al., 2025)*. Recovery efficiencies below about 50% are generally regarded as insufficient for sustainable ATES operation *(Bloemendal & Hartog, 2018)*. For this reason, a threshold of $\eta \geq 0.5$ is adopted here as a conservative criterion, ensuring that ATES operation remains financially interesting and supports optimal and sustainable subsurface use.

Taken together, the dual criteria of $\Delta T_{supply} \leq 0.5$ °C at the extraction well and $\eta \geq 0.5$ for the ATES system provide complementary perspectives on groundwater safety and energy efficiency. This combined framework ensures that both environmental protection and practical performance targets are consistently integrated into the assessment of ATES impacts.

3. Results

Results are presented separately for the three scenarios defined in Section 2.4. For each scenario, model outputs include the simulated temperature time series at the extraction well for different distances, as well as the thermal recovery efficiency of both warm and cold wells. To systematically explore the main controlling factors, DGSA was applied and the results are reported in terms of sensitivities for individual parameters as well as pairwise interactions.

3.1. Scenario 1: Single balanced system

Scenario 1 considers a single ATES doublet operated in perfectly balanced seasonal cycles, simulated for five years. The extraction-well temperature illustrates the contrasting near- and far-field responses (Figure 2(a) and (d)). At 75 m, the extraction well shows a clear seasonal cycle: the difference between summer peaks and winter minima is about 1.2 °C, corresponding to a seasonal increase and subsequent decrease of roughly ±0.6 °C around the mean. At 200 m, this seasonal range shrinks to about 0.5 °C, indicating a substantial attenuation of the thermal plume with distance. For each distance, two clusters of realizations are identified, with a high-disturbance cluster whose seasonal temperature curves lie systematically about 0.1 °C above those of the low-disturbance cluster. These differences between and within the two clusters show that uncertainty in aquifer and operational parameters leads to measurable differences in the seasonal temperature disturbance at the

supply well.

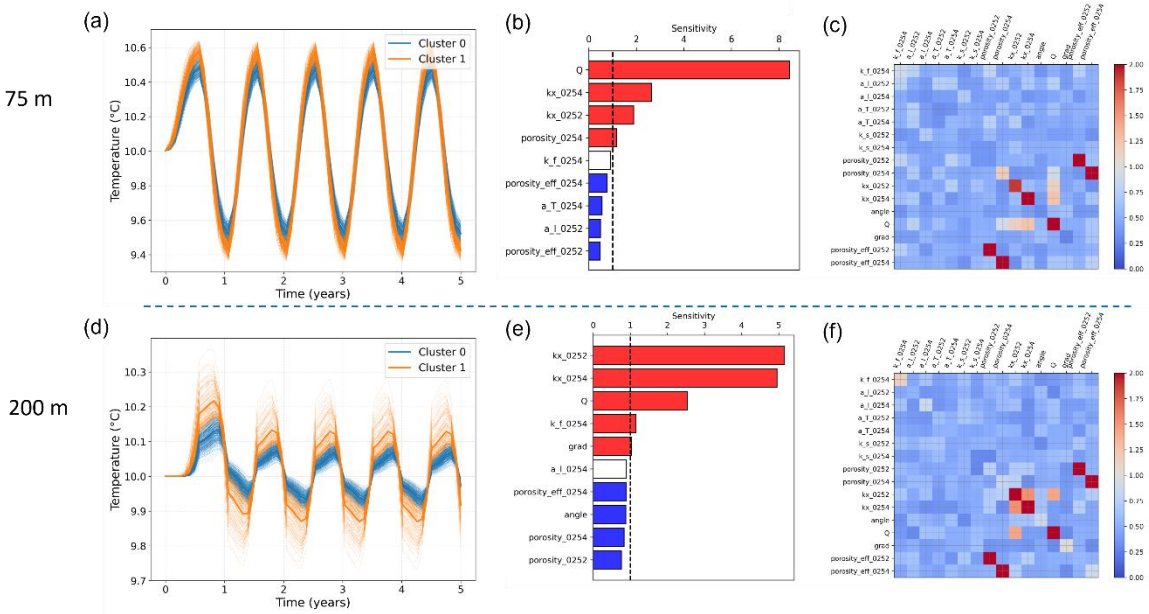

Figure 2: Temperature at the public-supply well located 75 m and 200 m from the ATES doublet (Scenario 1). (a) Clustered temperature variation at 75 m (Cluster 0 = lower disturbance, Cluster 1 = higher disturbance); (b) Parameter sensitivity ranking at 75 m; (c) Interaction sensitivity at 75 m; (d) Clustered temperature variation at 200 m; (e) Parameter sensitivity ranking at 200 m; (f) Interaction sensitivity at 200 m. In (c) and (f), diagonal cells repeat the corresponding first-order sensitivities and are not interpreted as parameter interactions.

The DGSA results reveal different relative sensitivities for each parameter for each distance (Figure 2 (b), (c), (e) and (f)). At 75 m, the ATES extraction/injection flow rate Q_{ATES} dominates the sensitivity ranking (index $\approx$ 8), because stronger pumping enhances forced convection, enlarges the effective thermal radius of the stored heat and allows the thermal plume to reach the supply well earlier and with a larger seasonal temperature disturbance. Aquifer conductivities of the pumped (kx_0254) and overlying (kx_0252) units follow as sensitive parameters, whereas the porosity of the pumped unit (porosity_0254) ranks low in the DGSA results and indicates at most a minor influence on the seasonal temperature range ΔT_{supply} at the supply well. At 200 m, however, operational influence weakens: the horizontal hydraulic conductivities kx_0254 and kx_0252 become the most influential parameters (indices $\gtrsim$ 5), while the flow rate Q_{ATES} drops to secondary relevance and the regional hydraulic gradient (grad) begin to contribute moderately. The fluid thermal conductivity in the pumped unit (k_f_0254) also shows a moderate sensitivity at this distance, consistent with the increasing relative importance of conductive heat transfer along the longer flow path once the direct pumping influence on the temperature signal has largely decayed. Second-order interaction effects show distinct patterns at 75 m and 200 m (Figures 2c, f). At 75 m, interaction indices are uniformly small (below 1) and substantially lower than the leading first-order sensitivities, with only weak interactions involving Q_{ATES} and the horizontal conductivities kx_0254 and kx_0252. This indicates that the near-field response of ΔT_{supply} is governed almost entirely by individual parameters, primarily the pumping rate and the

transmissivity of the pumped unit, with little additional variance explained by their combinations. At 200 m, interaction strengths increase slightly but remain secondary: a few parameter pairs that involve kx_0254 and kx_0252, as well as their effective porosities, attain standardized interaction values just above 1, while Q_{ATES} shows a noticeable interaction mainly with kx_0252. These patterns suggest that in the far field the joint influence of transmissivity and storage in the pumped and overlying units controls how the thermal plume both spreads along the regional flow path and exchanges heat with the overlying aquifer.

Scatter plots support the distance-dependent controls on the maximum seasonal temperature difference at the public-supply well, ΔT_{supply} (Figure 3). At R = 75 m (Figure 3a-d), ΔT_{supply} increases nearly linearly with the ATES injection/extraction rate Q_{ATES} ($\approx$+0.1 °C per +10 m^3h^{-1}, Figure 3a), confirming that thermal disturbance scales with the injected water volume. In contrast, relationships with the horizontal hydraulic conductivity of the pumped aquifer (kx_0254) and the overlying unit (kx_0252) and local flow intensity are comparatively weak at 75 m and mainly expressed as spread across realizations (Figure 3b-d). At R = 200 m, the dependence on Q_{ATES} is weaker and more scattered (Figure 3e), while clearer structure emerges with aquifer properties: higher kx_0254 is associated with slightly larger ΔT_{supply} and reduced variability, whereas higher kx_0252 tends to lower ΔT_{supply} (Figure 3f-g). ΔT_{supply} also increases with the local Darcy flux (specific discharge) evaluated near the public-supply well (Figure 3h), which reflects the combined influence of hydraulic conductivity and the local hydraulic gradients. A transition is observed around ~4.2×10^{-4} m s^{-1} of breakpoint: realizations below this value mainly fall in the 0.1-0.3 °C range, whereas higher values consistently yield $\Delta T_{supply}\approx$0.3-0.6°C. Overall, the scatter plots indicate that near-field disturbance is primarily controlled by operational throughput, whereas far-field variability is more closely linked to aquifer properties and local flow intensity.

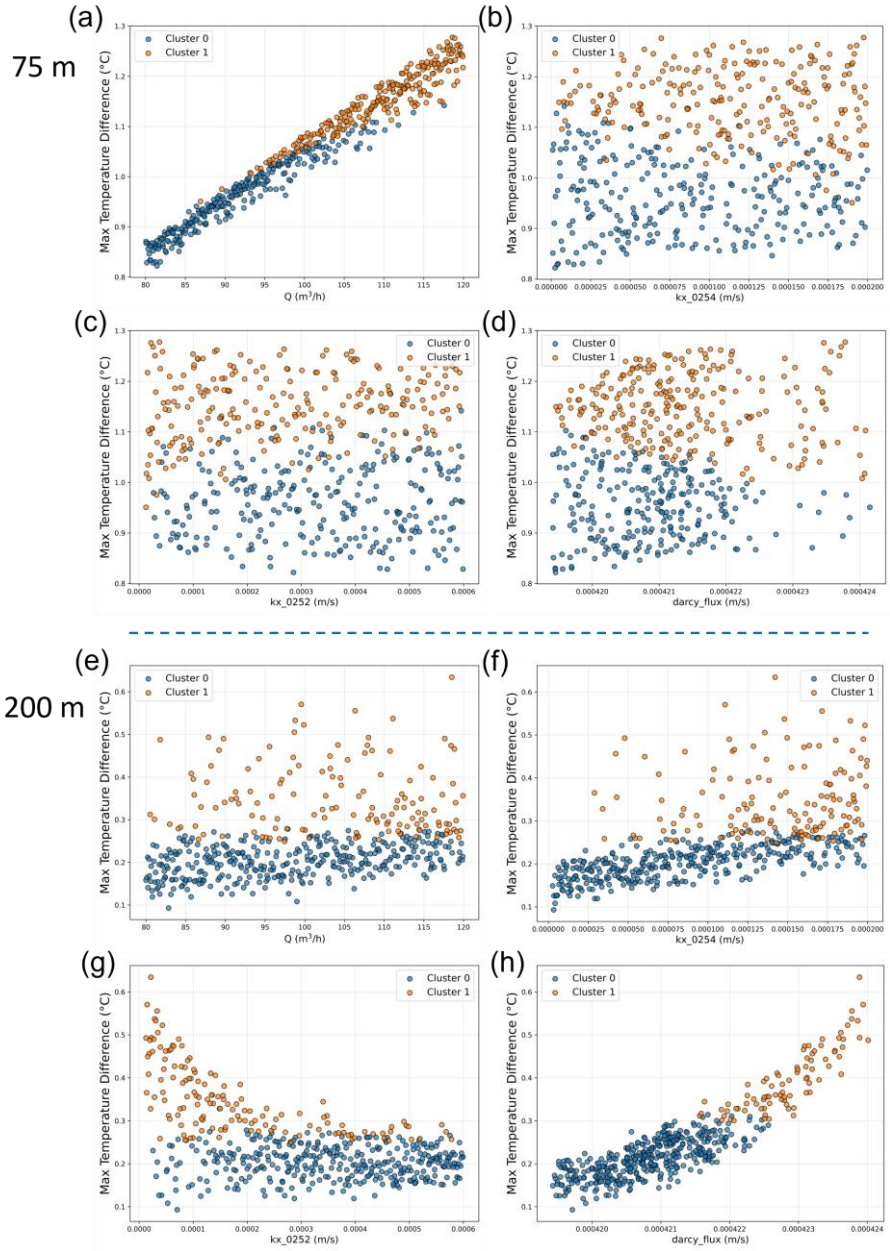

412

413 *Figure 3: Relationships for Scenario 1 between sensitive parameters and maximum temperature*
414 *difference (ΔT_{supply}) at the public-supply well near ATES (75 m and 200 m). (a-d) Scatter plots at 75*
415 *m showing effects of flow rate Q, kx_0252, kx_0254, and Darcy flux; Cluster 0 = low disturbance,*
416 *Cluster 1 = high disturbance; (e-h) Scatter plots at 200 m showing effects of flow rate Q, kx_0252,*
417 *kx_0254, and Darcy flux.*

418 The thermal recovery efficiency results are shown in Figures 4-5. Efficiency is computed
419 separately for the warm and cold wells; here we report the warm-well results for Scenario 1,
420 since warm- and cold-well efficiencies show comparable behavior under balanced operation.
421 Values are shown as the annual mean recovery efficiency (one mean value per simulation
422 year), yielding a five-point time series over the five-year simulation (Figure 4a in 75m and
423 200m). DGSA identifies the ATES injection/extraction rate Q_{ATES}, the horizontal hydraulic
424 conductivity of the pumped aquifer (kx_0254), and the hydraulic conductivity of the

overlying unit (kx_0252) as the dominant controls on recovery efficiency. At R = 75m, efficiencies stabilize quickly and span ~0.10-0.30, with a lower-efficiency range (~0.10-0.18) and a higher-efficiency range (~0.20-0.30) (Figure 4a). Higher Q_{ATES} is associated with higher recovery because a larger seasonal injected-extracted volume strengthens recirculation between the warm and cold wells and keeps a larger fraction of the stored heat within the ATES capture zone for subsequent pumping. In contrast, higher kx_0254 tends to reduce recovery by increasing lateral flow capacity in the pumped layer, which stretches the thermal plume and promotes advective heat export away from the wells (Figure5 a,d). Higher kx_0252 shows the opposite effect: recovery increases with kx_0252 (Figure 5b,e), consistent with a larger fraction of heat being redistributed into the overlying unit rather than remaining concentrated in the pumped layer, thereby reducing lateral heat loss along the main flow path in 0254 and supporting later recapture. At R = 200 m, efficiencies shift to higher values (~0.40-0.60), and sensitivity to Q_{ATES} becomes weak; outcome separation is governed mainly by kx_0254 and kx_0252, with longitudinal dispersivity (a_l), effective porosity, and the fluid thermal conductivity (k_f) contributing secondarily (Figure 4c). These secondary effects are consistent with enhanced spreading and mixing: larger a_l smears the thermal front and reduces the contrast of the recovered signal, while effective porosity modifies pore-water velocities and residence times, and higher k_f promotes conductive spreading that becomes relatively more relevant over longer travel paths. Scatter plots in Figure 5 illustrate the dominant trends across both distances: recovery decreases with increasing kx_0254 (Figure 5a,d), increases with kx_0252 (Figure 5b,e), and shows the clearest negative correlation with the local Darcy flux (specific discharge) (Figure 5c,f), indicating that stronger local throughflow enhances advective heat export from the storage volume. Under this prescribed pumping configuration, the regional hydraulic gradient does not emerge as an influential parameter for recovery efficiency in DGSA (Figure 4), suggesting that variability in recovery is explained primarily by aquifer flow capacity and local flow intensity around the storage volume. Overall, operational throughput primarily shapes recovery in the near field, whereas at larger setback distances recovery is governed mainly by aquifer flow capacity and the resulting flow intensity.

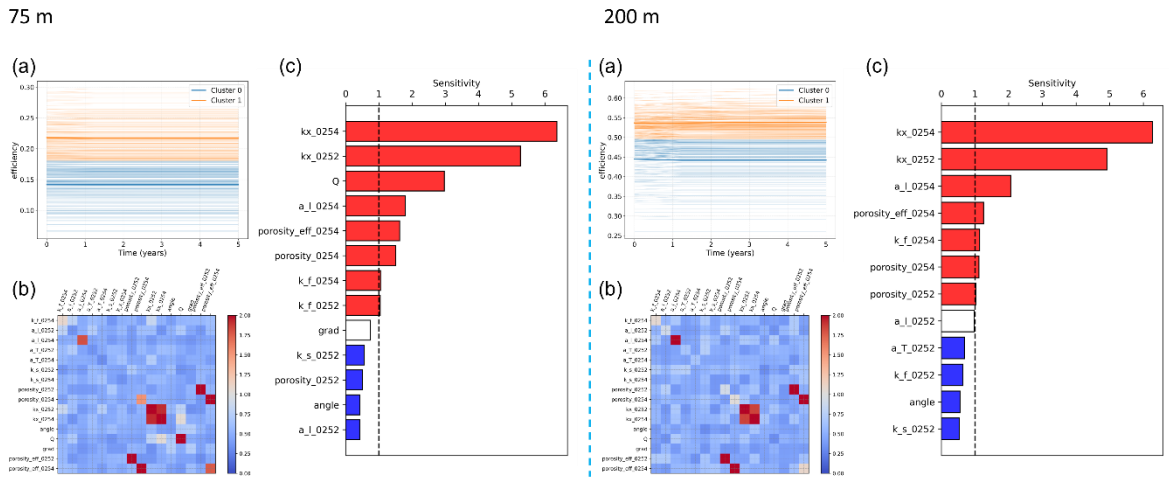

Figure 4: Clustering and sensitivity analysis of ATES thermal recovery efficiency for Scenario 1 at 75 m and 200 m distances. (a-c) Warm well at 75 m: clustered efficiency time series (Cluster 0 = low efficiency, Cluster 1 = high efficiency), parameter sensitivity ranking, and parameter interaction heatmap; (d-f) Warm well at 200 m: clustered efficiency time series, parameter sensitivity ranking, and parameter interaction heatmap.

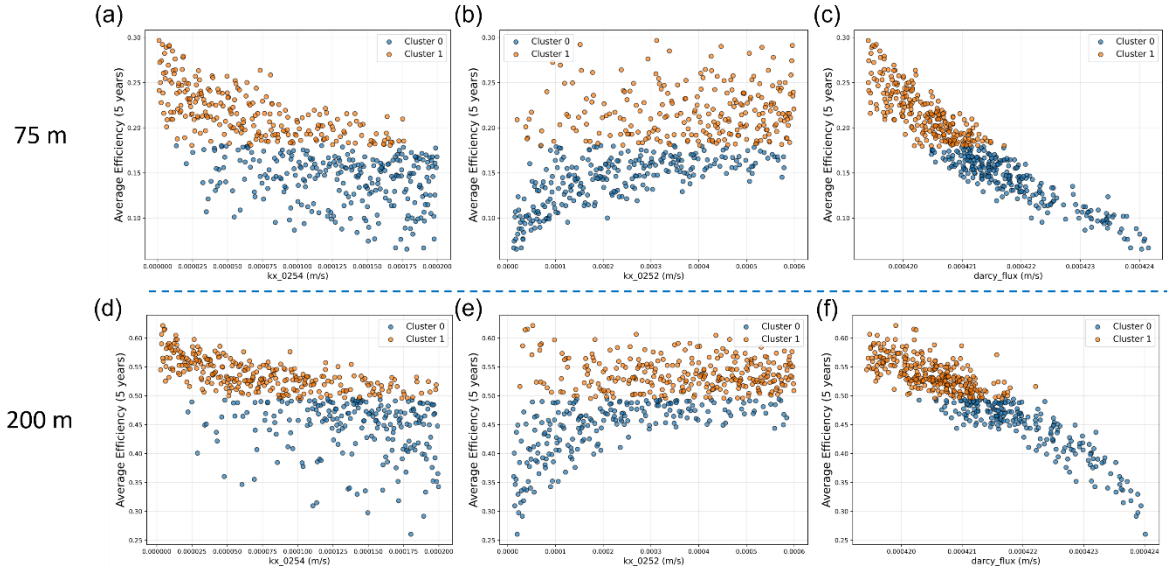

Figure 5: Relationships for Scenario 1 between sensitive parameters and average thermal recovery efficiency of the ATES warm well at 75 m and 200 m. (a-c) Scatter plots at 75 m showing effects of kx_0254, kx_0252, and Darcy flux on efficiency (Cluster 0 = low efficiency, Cluster 1 = high efficiency); (d-f) Scatter plots at 200 m showing effects of kx_0254, kx_0252, and Darcy flux on efficiency.

In summary, Scenario 1 illustrates a clear near-to-far-field transition in governing mechanisms. At short distance (75 m), both the thermal disturbance at the public-supply well and recovery efficiency are primarily controlled by operational throughput, with aquifer properties playing a secondary role. At the larger distance (200 m), plume spreading and geological contrasts become the main sources of variability, and recovery generally increases relative to 75 m as direct short-circuiting and near-field interference are reduced. Importantly, however, the magnitude of recovery at 200 m remains linked to the local flow intensity around the storage volume (as captured by the local Darcy flux), which reflects the combined effect of aquifer flow capacity and the prescribed pumping-induced flow field of the public-supply well. The gradual transition with increasing distance is further supported by the intermediate-distance results considered in Scenario 2 (175-300 m), which capture the buffering regime between the near field and the far field

3.2. Scenario 2: Single system under seasonally imbalanced operation

Scenario 2 evaluates a single ATES doublet operated under seasonally imbalanced cycles, where summer injection exceeds winter extraction by up to 50%. Compared to balanced operation (Scenario 1), the public-supply well shows a larger and more asymmetric

seasonal temperature disturbance in the near field (Figure 6). At R=75 m, the peak-to-trough seasonal temperature range is about 1.5 °C, exceeding the ~1.2 °C range under balanced operation. Summer peaks become sharper under net heat injection, whereas winter minima are broader, reflecting a more prolonged cooling/recovery phase. Two response groups (lower vs higher disturbance) remain visible, indicating that seasonal imbalance amplifies the spread in outcomes across realizations.

Based on the distance dependent behavior observed in Scenario 1, Scenario 2 explicitly treats the distance (R) as an uncertain input for the "far-field" analysis. Accordingly, the second set of simulations samples multiple distances in the range R=(175-300) m (Figure 6d-f), capturing the transition from near-field interference to far-field buffering. Across this range, the seasonal temperature disturbance decreases with increasing (R) and converges to a small peak-to-trough range of ~0.2-0.3°C at the larger distances. Importantly, over the five simulated years, the temperature time series do not show a progressive upward shift, there is no clear cumulative warming trend despite the seasonal imbalance.

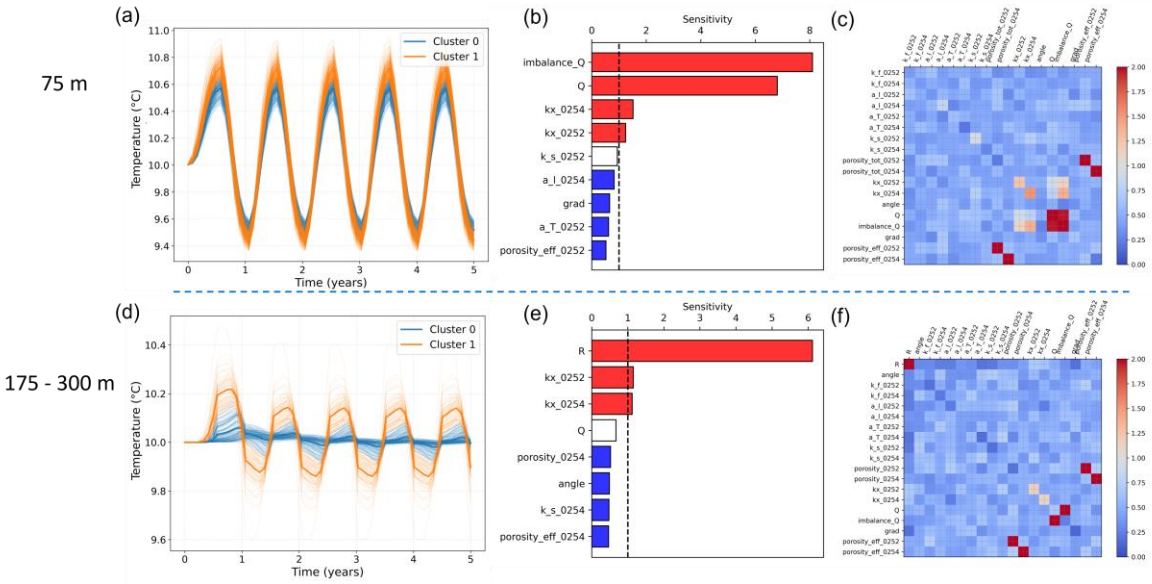

Figure 6: Extraction well temperature response and sensitivity under seasonal imbalance conditions near ATES at 75 m and 175-300 m. (a-c) At 75 m: clustered temperature variation, sensitivity ranking of parameters, and parameter interaction heatmap; (d-f) At 175-300 m: clustered temperature variation, sensitivity ranking of parameters, and parameter interaction heatmap.

DGSA indicates a clear shift in parameter control under seasonal imbalance (Figure 6). At R=75 m, the imbalance-related flow component (imbalance Q) is the dominant driver of T_{supply} (sensitivity ≈ 8), closely followed by the ATES injection/extraction rate Q_{ATES} (≈ 7), while aquifer hydraulic conductivities in the pumped and overlying units (kx_0254 and kx_0252) have secondary influence (~1-1.5). Other parameters contribute little to the variability of the near-field temperature response.

For the far-field analysis, distance between ATES and supply-well (R) is explicitly included as an input and sampled across R=175-300 m to capture the transition regime identified in Scenario 1. Accordingly, DGSA ranks R as the dominant control in this range (sensitivity ≈ 6), with contrasting hydraulic conductivity fields (kx_0254 and kx_0252) regaining

importance, whereas operational parameters fall below the sensitivity threshold. This confirms that increasing spacing systematically damps the supply-well temperature disturbance under imbalance and shifts the system response from operation-controlled to geology-controlled behavior. Supporting scatter relationships are provided in Appendix (Fig. A1).

System efficiency diverges between warm and cold wells under seasonal imbalance (Figure 7). At R=75 m, the warm well benefits from net heat injection, with annual mean efficiency increasing to ~0.25-0.35 compared to ~0.15-0.25 under balanced operation. The cold well shifts to lower efficiencies (~0.10-0.20), consistent with earlier thermal breakthrough and reduced temperature contrast in the recovery zone under imbalanced cycling. DGSA confirms this asymmetry: at 75 m, both warm- and cold-well efficiencies are primarily controlled by the imbalance parameter (imbalance Q) and the ATES injection/extraction rate Q_{ATES}, with aquifer conductivities (kx_0254 and kx_0252) as key secondary controls (Figure 7b,e). For the cold well, additional parameters contribute at a secondary level, indicating a higher sensitivity of cold recovery to hydrogeological variability under imbalance (Figure 7e,f).

For the transition-range analysis (R=175-300 m), warm- and cold-well efficiencies converge to similarly higher values (both ~0.45-0.55; Figure 7g-l). In this regime, distance R emerges as a dominant control and geological contrasts regain importance, while operational parameters become less influential, indicating that increased spacing mitigates the near-field impact of seasonal imbalance under the prescribed pumping regime. Supporting parameter response relationships are provided in the Appendix (Figure A2).

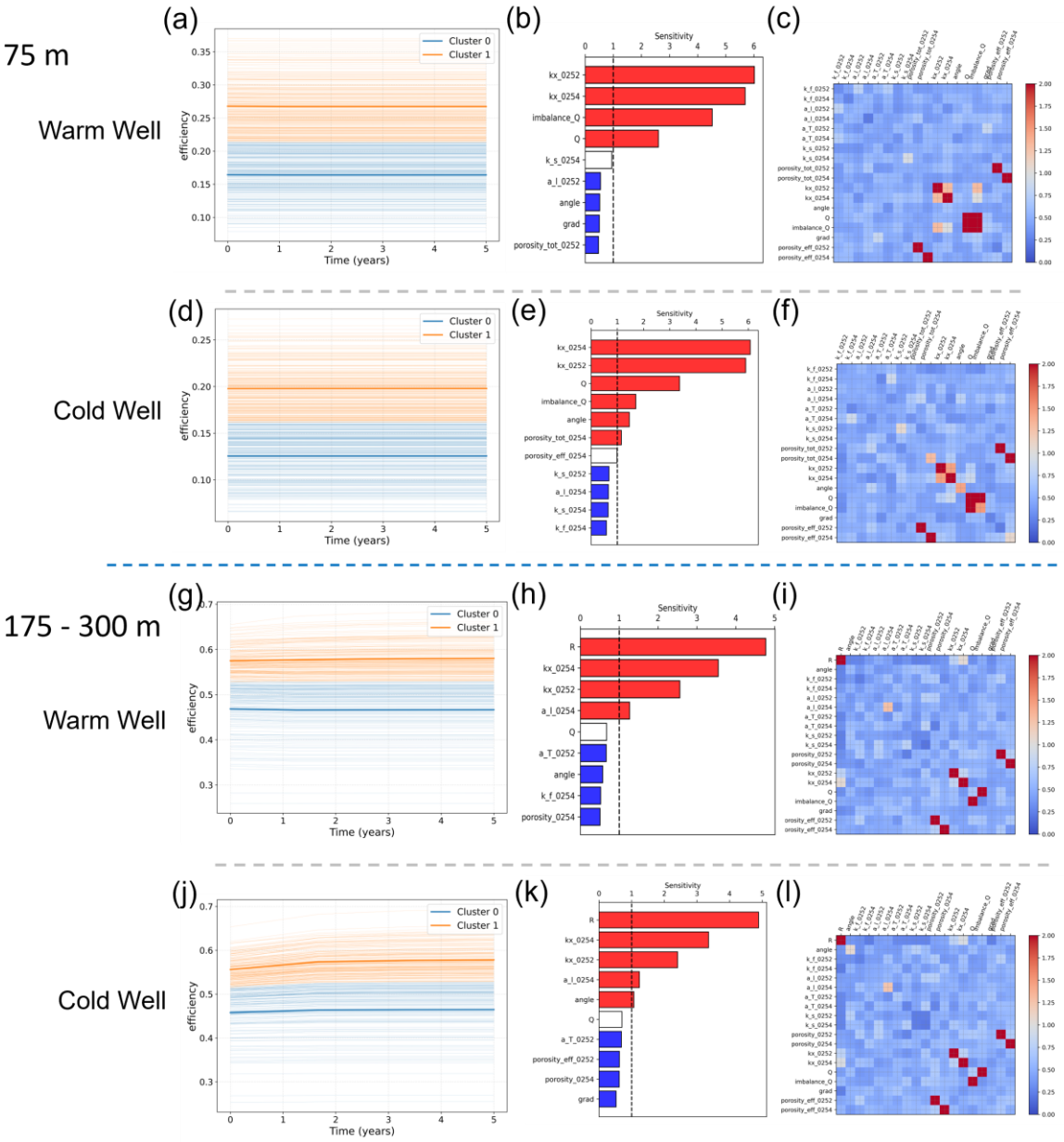

Figure 7: Clustering and sensitivity analysis of ATES thermal recovery efficiency under seasonal imbalance conditions at 75 m and 175-300 m. (a-c) Warm well at 75 m: clustered efficiency (Cluster 0 = low efficiency, Cluster 1 = high efficiency), sensitivity ranking of parameters, and parameter interaction heatmap; (d-f) Cold well at 75 m: clustered efficiency, sensitivity ranking of parameters, and parameter interaction heatmap; (g-i) Warm well at 175-300 m: clustered efficiency, sensitivity ranking of parameters, and parameter interaction heatmap; (j-l) Cold well at 175-300 m: clustered efficiency, sensitivity ranking of parameters, and parameter interaction heatmap.

In summary, seasonal imbalance leads to larger near-field T_{supply} and a stronger warm cold efficiency asymmetry. With increasing setback distance, disturbances decrease and efficiencies converge, while geological contrasts become more important under the prescribed supply-well pumping regime.

3.3. Scenario 3: Multiple systems under seasonally imbalanced operation

Scenario 3 examines multi-ATES operation under seasonal imbalance at a short distance of 75 m to represent the most critical near-field interference case. (At larger distances, the attenuation of thermal impacts with distance is already characterized in Scenarios 1 and 2, therefore, the multi-system analysis is focused on the dense-layout worst case.) Two deployment layouts were considered to represent contrasting field practices (Tas et al., 2023): a checkerboard layout, where warm and cold wells alternate in both horizontal directions, and a lane layout, where warm and cold wells are aligned along one axis. The layout is implemented as a categorical Monte Carlo input (pattern), such that realizations are evaluated for either checkerboard or lane configurations.

At the public-supply well, the multi-system setting produces the largest seasonal temperature disturbance of the study (Figure 8a). Temperatures fluctuate around ~10 °C with a peak-to-trough range approaching 3 °C, substantially exceeding the single-system response. Two consistent temperature time series types are observed: in the high-disturbance cases, warm plumes from neighboring doublets overlap and reinforce during the warm season, leading to sustained peaks above 11 °C; in the low-disturbance cases, plume contributions overlap less strongly and the peaks are shorter and lower.

DGSA shows that, as in Scenario 2, the dominant controls on T_{supply} are operational (imbalance and Q_{Ates}) (Figure 8b,c). Aquifer conductivities (kx_0254 and kx_0252) act as secondary modifiers by influencing advective spreading in the pumped layer and vertical exchange with the overlying unit. The layout (pattern) has only a minor influence on the supply-well temperature response, indicating that plume interference dominates the signal. Over the simulated period, no progressive upward drift in temperature is observed.

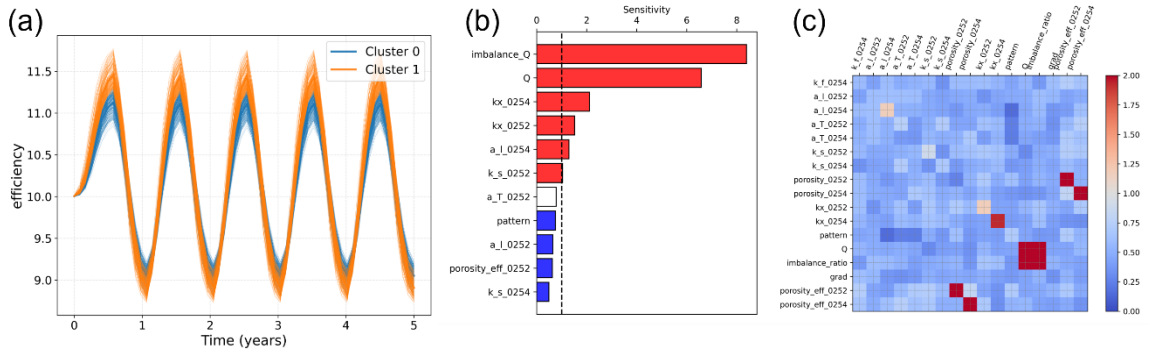

Figure 8: Extraction well temperature response and sensitivity under multiple ATES systems with seasonal imbalance (75 m). (a) Clustered temperature variation at the extraction well (Cluster 0 = low disturbance, Cluster 1 = high disturbance); (b) Sensitivity ranking of parameters controlling maximum temperature difference (ΔT); (c) Interaction sensitivity heatmap of parameters.

Efficiency results for the four ATES wells show a pronounced asymmetry under dense, seasonally imbalanced operation (Figure 11). The two warm wells behave similarly, with annual mean efficiencies mainly within ~0.20-0.30 and sensitivities dominated by Q_{ATES}, the imbalance parameter (imbalance Q), and aquifer conductivities. The two cold wells show contrasting behavior. Cold well 1 exhibits a relatively narrow efficiency range, whereas cold well 2 shows systematically lower and more variable efficiencies. This behavior is consistent with repeated thermal intrusion into the capture zone of cold well 2 due to its position relative

to neighboring warm wells and the regional flow direction, leading to earlier thermal breakthrough. Sensitivity patterns for cold well 2 reflect this (Figure 9): aquifer conductivities play a major role in controlling plume spreading and vertical exchange, while sensitivity to Q_{ATES} is comparatively weak. The pattern (checkerboard versus lane), negligible for the supply-well temperature response, becomes relevant for cold well 2 because it changes the degree of plume overlap at that location and thereby affects recovery efficiency.

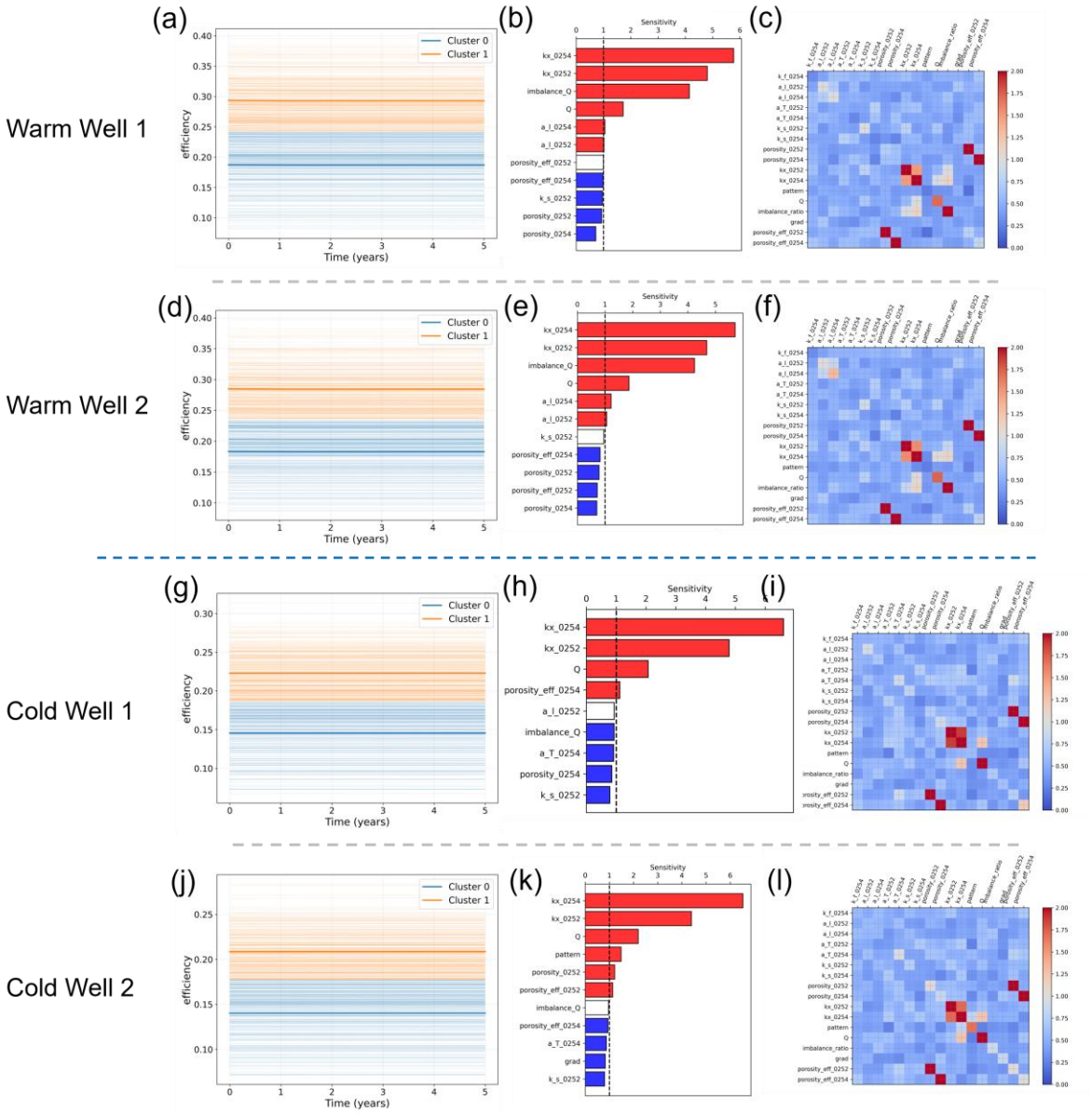

Figure 9: Clustering and sensitivity analysis of ATES well efficiency under multiple systems with seasonal imbalance (75 m).(a-c) Warm well 1: clustered efficiency (Cluster 0 = low efficiency, Cluster 1 = high efficiency), parameter sensitivity ranking, and parameter interaction heatmap; (d-f) Warm well 2: clustered efficiency, parameter sensitivity ranking, and parameter interaction heatmap; (g-i) Cold well 1: clustered efficiency, parameter sensitivity ranking, and parameter interaction heatmap; (j-l) Cold well 2: clustered efficiency, parameter sensitivity ranking, and parameter interaction heatmap..

Taken together, dense multi-system operation under seasonal imbalance produces the largest temperature disturbance and variability at the public-supply well and increases efficiency asymmetry across ATES wells, with the cold wells (especially cold well 2) most affected. The dominant controls remain operational forcing and aquifer conductivities, while plume interference among neighboring ATES doublets is the primary driver of risk, with layout effects secondary.

4. Discussion

This study reveals a coherent picture of how ATES operation perturbs drinking-water wells across distances, seasonal regimes, and spatial deployment densities. At short separation distances ($\leqslant$75 m), thermal response at the supply well is dominated by pumping-induced forced convection arising from both ATES cycling and continuous drinking-water abstraction. Larger ATES flow rate (Q_{ATES}) and summer imbalance (imbalance_Q) primarily amplify peak ΔT_{supply} (i.e., cluster separation is mainly range-driven), yielding near-linear ΔT_{supply}-Q_{ATES} relations and the widest separation between response clusters. Continuous drinking water abstraction further enhances this effect by hydraulically short-circuiting heat transport, so that injected heat is rapidly flushed toward the supply well rather than accumulating in the aquifer (Zuurbier et al., 2014). This mechanism also explains why no long-term warming or temperature drift was observed in imbalanced Scenarios 2 and 3: abstraction exports the net thermal surplus and associated warm/cold plume out of the ATES capture/recovery zone, preventing accumulation near the recovery wells.

With increasing distance ($\geqslant$200 m), advection remains important, particularly under the capture field imposed by the drinking-water well, but the dominant sources of variability shift toward plume spreading and vertical exchange. Geological contrasts, particularly the horizontal conductivities of the pumped (kx_0254) and overlying (kx_0252) units, become the primary controls, and the natural regional gradient contributes to residual variability. Higher kx_0254 confines heat within the pumped horizon, sustaining longitudinal advection and elevating $\Delta T_{supplly}$ at the supply well, whereas higher kx_0252 promotes vertical sharing and leakage that dilute the signal (Bonte, Stuyfzand, Hulsmann, et al., 2011). The observed Darcy-flux break (~4.2×10^{-4} m s^{-1}) provides a practical divider between dispersion-limited responses (~0.1-0.2 °C) and advection-enhanced responses (~0.3-0.6 °C), consistent with tracer-based studies of aquifer transport (Anderson, 2005).

Efficiency patterns complement, and sometimes counterpoint, the ΔT_{supply} behavior. In the near field, net summer loading increases warm-well recovery but depresses cold-well recovery, producing asymmetric performance. In multi-system cases, cold wells, particularly those located downstream of overlapping plumes, show the lowest and most variable efficiency, as illustrated by cold well 2 in Scenario 3. At larger distance, both warm and cold wells improve and converge to ~0.5-0.6, with aquifer conductivities and distance becoming the primary determinants. Importantly, this indicates a trade-off: conditions that enhance recovery (higher kx_0254, higher Darcy flux, closer spacing, stronger imbalance) also elevate ΔT_{supply} at the supply well, whereas layouts that minimize ΔT_{supply} may yield lower recovery. We therefore recommend a multi-objective siting and permitting approach that

prioritizes setback distance as the first-line risk control and, where distance is constrained, explicitly constrains ATES flow rate (Q_{ATES}) and seasonal imbalance (imbalance_Q) to meet the drinking-water well temperature criterion while preserving acceptable recovery.

Consistent with this recommendation, the results suggest that distances of ~200-300 m effectively limit ΔT_{supply} at the supply well to natural background variability ($\leqslant$0.5 °C) (Figure 10), even under imbalanced or multi-system operation. Accordingly, we propose a tiered guideline: (i) ~300 m as a preferred distance that combines groundwater protection with stable ATES recovery; (ii) ~200 m as a minimum distance to keep thermal disturbances within natural annual temperature range (Anderson, 2005); and (iii) <200 m only if stricter operational controls are imposed, most importantly limits on Q_{ATES} and imbalance_Q_{ATES}, to avoid exceedance of thermal thresholds. Although Figure 10 illustrates the balanced case, similar attenuation of ΔT_{supply} and convergence of efficiency with distance were observed across scenarios, supporting the robustness of distance-dependent buffering.

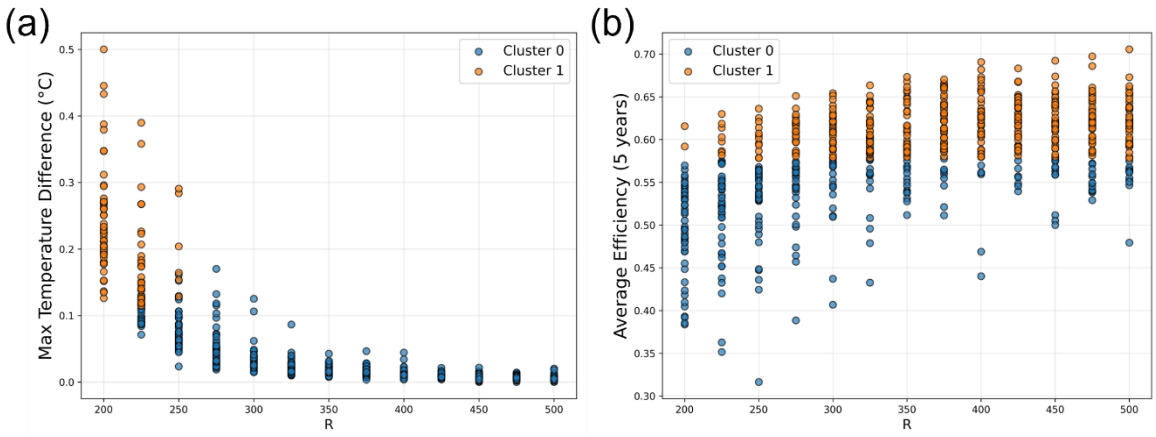

Figure 10: Effect of ATES-extraction well distance (R) on thermal disturbance and system efficiency.(a) Maximum temperature difference (ΔT) at the extraction well vs. distance R (Cluster 0 = low disturbance, Cluster 1 = high disturbance); (b) Average thermal recovery efficiency of the ATES warm well vs. distance R (Cluster 0 = low efficiency, Cluster 1 = high efficiency).

The main contribution of this work is a transferable assessment workflow, which combines a dual performance metric (ΔT_{supply} at drinking-water well and ATES recovery efficiency) with scenario-based uncertainty analysis and DGSA to identify controls under single- and multi-system deployment. The numerical thresholds reported here (e.g., distances and Darcy-flux breakpoints) should be interpreted as case-dependent, and are therefore most directly applicable to the Campine Basin and aquifers with comparable stratification and conductivity contrasts. For other aquifers, the recommended practice is to reuse the approach to derive site-specific thresholds using local hydrogeology, operational envelopes, and protection criteria.

Key limitations affecting broader application include the representation of drinking-water production as a single extraction well, whereas real-world supply typically involves wellfields with time-varying pumping and more complex capture zones. This simplification may shift predicted transport pathways and thus modify minimum distance requirements, future work should explicitly represent wellfields and explore pumping variability. In

addition, the model idealizes subsurface properties (homogeneous and isotropic units) and does not include coupled hydrogeochemical processes; incorporating heterogeneity, anisotropy, and reactive transport, especially where ATES wells penetrate confining layers, would improve the robustness of risk estimates. Finally, field monitoring at operating ATES-abstraction settings is needed to validate the inferred Darcy-flux threshold and to refine distance guidance under real-world heterogeneity.

Overall, for settings comparable to the Campine Basin, distances on the order of 200-300 m emerge as an effective first-line risk control. Where space is limited, permitting should rely on operational levers (throughput and seasonal imbalance) and account for vertical conductivity contrasts during site selection, using the conservative criterion as a compliance benchmark compatible with drinking-water protection while enabling ATES deployment.

5. Conclusion

This study combined groundwater flow and heat-transport modeling with distance-based generalized sensitivity analysis to quantify ATES-supply well interactions in the Campine Basin.

1. Thermal impacts at public-supply wells are strongest at short distances and attenuate substantially with increasing distance.
2. In the near field ($\leqslant$75 m), peak ΔT_{supply} is primarily controlled by ATES flow rate (Q_{ATES}) and seasonal imbalance under pumping-induced convection from ATES cycling superimposed on continuous supply-well abstraction.
3. In the far field ($\geqslant$200 m), response variability is governed mainly by aquifer property contrasts together with regional gradients and the hydraulic gradient induced by supply-well pumping.
4. Recovery efficiency generally improves with larger distance but is reduced by strong background flow and tight layouts, indicating a persistent performance-protection trade-off.
5. Practically, distances on the order of a few hundred meters provide an effective first-line risk control, and where distance is constrained, permitting should rely on limits on Q_{ATES} and seasonal imbalance.

Acknowledgement

This work was supported by the DIAMONDS project (FWO grant number: grant number S001324N).

Appendix

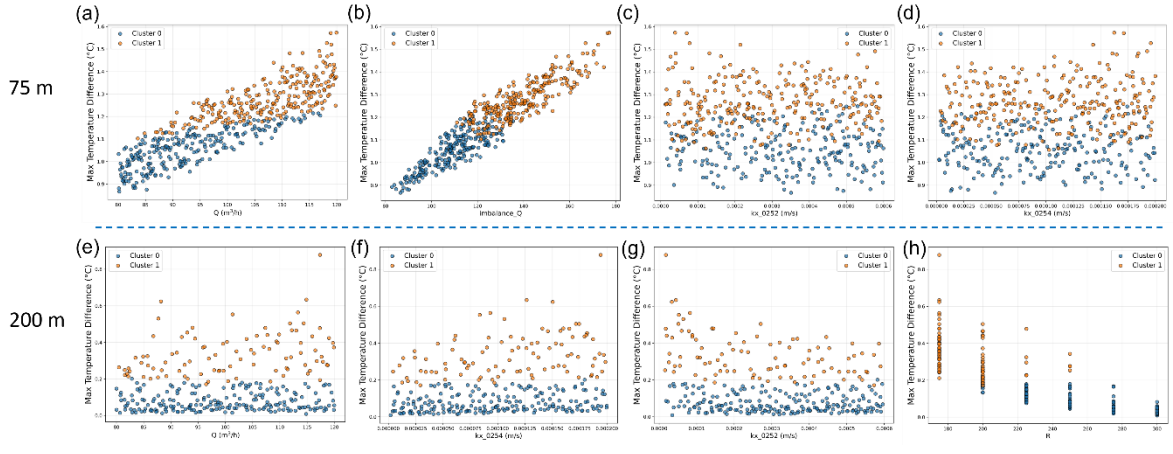

Figure A1: Relationships between sensitive parameters and maximum temperature difference (ΔT_{supply}) at the extraction well under seasonal imbalance conditions. (a-d) At 75 m: effects of flow rate Q_{ATES}, imbalance ratio (imbalance_Q_{ATES}), kx_0252, and kx_0254 on ΔT_{supply}); (e-h) At 175-300 m: effects of flow rate Q_{ATES}, imbalance ratio (imbalance_Q_{ATES}), kx_0252, and distance R on ΔT_{supply}.

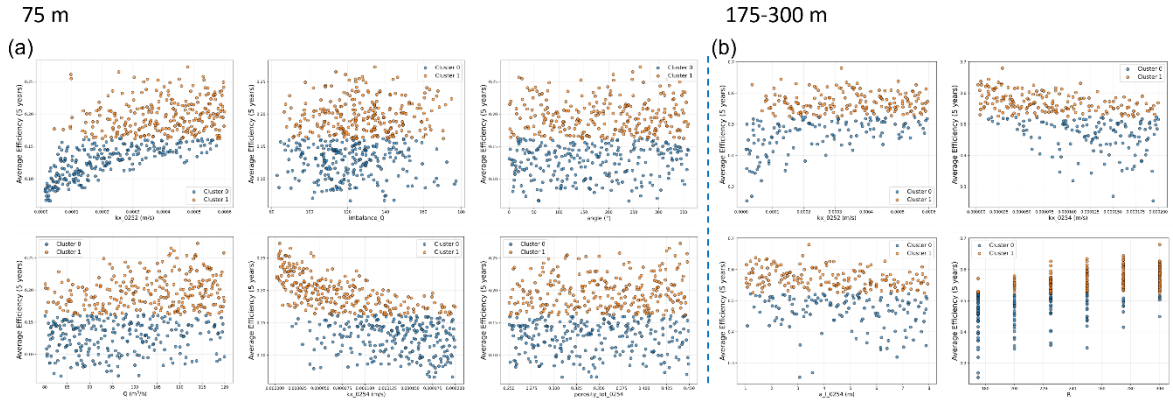

Figure A2: Relationships between sensitive parameters and average thermal recovery efficiency of the ATES cold well under seasonal imbalance conditions. (a-e) At 75 m: effects of flow rate Q, imbalance ratio (imbalance_Q), kx_0254, kx_0252, and angle on efficiency (Cluster 0 = low efficiency, Cluster 1 = high efficiency); (f-i) At 175-300 m: effects of kx_0254, kx_0252, longitudinal dispersivity (a_l_0254), and distance R on efficiency.

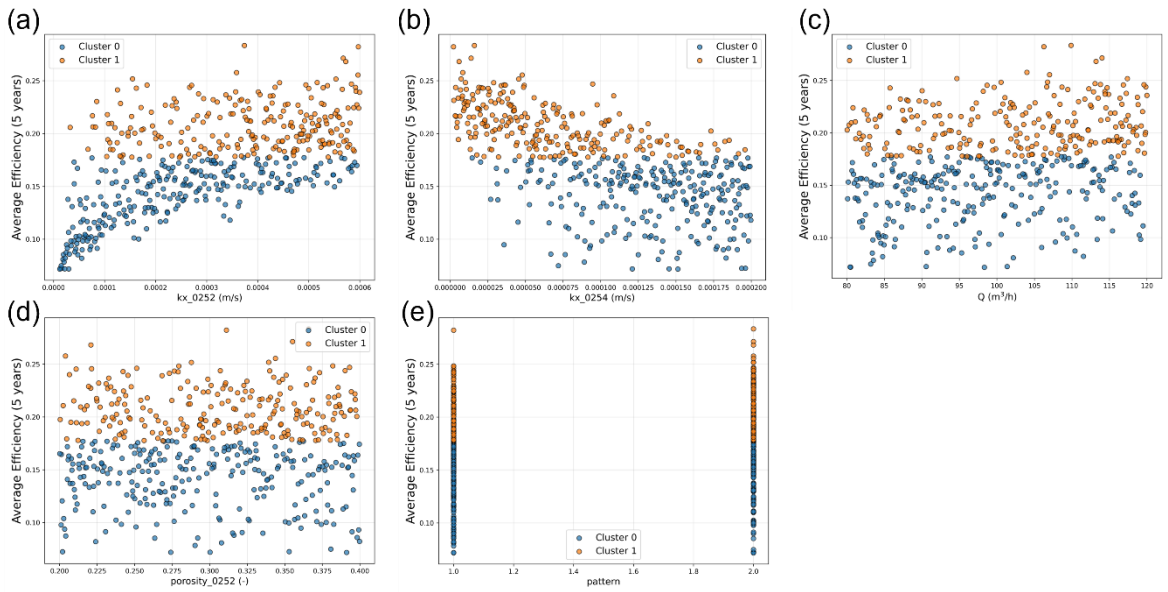

Figure A3: Relationships between sensitive parameters and average thermal recovery efficiency of ATES Cold well 2 under multiple systems with seasonal imbalance (75 m).(a-e) Effects of kx_0252, kx_0254, flow rate Q, porosity_0252, and system layout pattern on efficiency (Cluster 0 = low efficiency, Cluster 1 = high efficiency).

731 References

732 Allen, R. D. (1983). *Relationship of regional water quality to aquifer thermal energy storage* (No.
733 PNL-4929). Pacific Northwest Lab., Richland, WA (USA). https://doi.org/10.2172/5443697
734 Anderson, M. P. (2005). Heat as a Ground Water Tracer. *Groundwater*, *43*(6), 951–968.
735 https://doi.org/10.1111/j.1745-6584.2005.00052.x
736 Baalousha, H. M. (2016). Using Monte Carlo simulation to estimate natural groundwater recharge in
737 Qatar. *Modeling Earth Systems and Environment*, *2*(2), 87. https://doi.org/10.1007/s40808-
738 016-0140-8
739 Bakker, M., Post, V., Langevin, C. D., Hughes, J. D., White, J. T., Starn, J. J., & Fienen, M. N. (2016).
740 Scripting MODFLOW Model Development Using Python and FloPy. *Groundwater*, *54*(5),
741 733–739. https://doi.org/10.1111/gwat.12413
742 Bloemendal, M., & Hartog, N. (2018). Analysis of the impact of storage conditions on the thermal
743 recovery efficiency of low-temperature ATES systems. *Geothermics*, *71*, 306–319.
744 https://doi.org/10.1016/j.geothermics.2017.10.009
745 Bloemendal, M., Jaxa-Rozen, M., & Olsthoorn, T. (2018). Methods for planning of ATES systems.
746 *Applied Energy*, *216*, 534–557. https://doi.org/10.1016/j.apenergy.2018.02.068
747 Bloemendal, M., & Olsthoorn, T. (2018). ATES systems in aquifers with high ambient groundwater
748 flow velocity. *Geothermics*, *75*, 81–92. https://doi.org/10.1016/j.geothermics.2018.04.005
749 Blum, P., Menberg, K., Koch, F., Benz, S. A., Tissen, C., Hemmerle, H., & Bayer, P. (2021). Is
750 thermal use of groundwater a pollution? *Journal of Contaminant Hydrology*, *239*, 103791.
751 https://doi.org/10.1016/j.jconhyd.2021.103791
752 Bonte, M. (2013). *Impacts of Shallow Geothermal Energy on Groundwater Quality: A*
753 *Hydrochemical and geomicrobial study of the effects of ground source heat pumps and*
754 *aquifer thermal energy storage* [PhD-Thesis – Research external, graduation internal]. Vrije
755 Universiteit.
756 Bonte, M., Stuyfzand, P., Hulsmann, A., & Van Beelen, P. (2011). Underground Thermal Energy
757 Storage: Environmental Risks and Policy Developments in the Netherlands and European
758 Union. *Ecology and Society*, *16*(1). https://doi.org/10.5751/ES-03762-160122
759 Bonte, M., Stuyfzand, P. J., van den Berg, G. A., & Hijnen, W. A. M. (2011a). Effects of aquifer
760 thermal energy storage on groundwater quality and the consequences for drinking water
761 production: A case study from the Netherlands. *Water Science and Technology*, *63*(9), 1922–
762 1931. https://doi.org/10.2166/wst.2011.189
763 Bonte, M., Stuyfzand, P. J., van den Berg, G. A., & Hijnen, W. A. M. (2011b). Effects of aquifer
764 thermal energy storage on groundwater quality and the consequences for drinking water
765 production: A case study from the Netherlands. *Water Science and Technology*, *63*(9), 1922–
766 1931. https://doi.org/10.2166/wst.2011.189
767 Borko, K., Brenčič, M., Savšek, Z., Knez, J., Vozelj, A., Kisel, G., & Rman, N. (2025). Insights into
768 Aquifer and Borehole Thermal Energy Storage Systems for Slovenia's Energy Transition.
769 *Energies*, *18*(5), 1019. https://doi.org/10.3390/en18051019
770 Brielmann, H., Griebler, C., Schmidt, S. I., Michel, R., & Lueders, T. (2009). Effects of thermal
771 energy discharge on shallow groundwater ecosystems. *FEMS Microbiology Ecology*, *68*(3),
772 273–286. https://doi.org/10.1111/j.1574-6941.2009.00674.x

Casillas-Trasvina, A., Rogiers, B., Beerten, K., Wouters, L., & Walraevens, K. (2022a). Characterizing groundwater heat transport in a complex lowland aquifer using paleo-temperature reconstruction, satellite data, temperature–depth profiles, and numerical models. *Hydrology and Earth System Sciences*, *26*(21), 5577–5604. https://doi.org/10.5194/hess-26-5577-2022

Casillas-Trasvina, A., Rogiers, B., Beerten, K., Wouters, L., & Walraevens, K. (2022b). Exploring the hydrological effects of normal faults at the boundary of the Roer Valley Graben in Belgium using a catchment-scale groundwater flow model. *Hydrogeology Journal*, *30*(1), 133–149. https://doi.org/10.1007/s10040-021-02423-y

Casillas-Trasvina, A., Rogiers, B., Beerten, K., Wouters, L., & Walraevens, K. (2024). Bayesian inference of coupled groundwater flow and radiogenic helium-4 production and transport at the catchment scale. *Science of The Total Environment*, *954*, 176510. https://doi.org/10.1016/j.scitotenv.2024.176510

Databank Ondergrond Vlaanderen. (n.d.). *Databank Ondergrond Vlaanderen (DOV) – Flemish Subsurface Database*. Retrieved November 5, 2025, from https://www.dov.vlaanderen.be/

Drinkwaterbalans voor Vlaanderen—2020. (n.d.). Retrieved May 15, 2025, from https://vmm.vlaanderen.be/publicaties/drinkwaterbalans-voor-vlaanderen-2020

European Commission. (2006). *Directive 2006/118/EC of the European Parliament and of the Council of 12 December 2006 on the protection of groundwater against pollution and deterioration*. http://data.europa.eu/eli/dir/2006/118/oj

EU-WFD. (2000). *Directive—2000/60—EN - Water Framework Directive—EUR-Lex*. https://eur-lex.europa.eu/eli/dir/2000/60/oj/eng

Flemish Government. (1984). *Decreet van 24 januari 1984 houdende maatregelen inzake het grondwater (Grondwaterdecreet).* https://vmm.vlaanderen.be/beleid/wetgeving/grondwaterdecreet_gecoordineerde_versie_tw.pdf

Griebler, C., Brielmann, H., Haberer, C. M., Kaschuba, S., Kellermann, C., Stumpp, C., Hegler, F., Kuntz, D., Walker-Hertkorn, S., & Lueders, T. (2016). Potential impacts of geothermal energy use and storage of heat on groundwater quality, biodiversity, and ecosystem processes. *Environmental Earth Sciences*, *75*(20), 1391. https://doi.org/10.1007/s12665-016-6207-z

Haehnlein, S., Bayer, P., & Blum, P. (2010). International legal status of the use of shallow geothermal energy. *Renewable and Sustainable Energy Reviews*, *14*(9), 2611–2625. https://doi.org/10.1016/j.rser.2010.07.069

Hähnlein, S., Bayer, P., Ferguson, G., & Blum, P. (2013). Sustainability and policy for the thermal use of shallow geothermal energy. *Energy Policy*, *59*, 914–925. https://doi.org/10.1016/j.enpol.2013.04.040

Hecht-Méndez, J., Molina Giraldo, N., Bayer, P., & Blum, P. (2009). *Heat transport modelling using the multi-species transport model MT3DMS*.

Jackson, M. D., Regnier, G., & Staffell, I. (2024). Aquifer Thermal Energy Storage for low carbon heating and cooling in the United Kingdom: Current status and future prospects. *Applied Energy*, *376*, 124096. https://doi.org/10.1016/j.apenergy.2024.124096

Langevin, C. D., Hughes, J. D., Banta, E. R., Niswonger, R. G., Panday, S., & Provost, A. M. (2017). Documentation for the MODFLOW 6 Groundwater Flow Model. In *Techniques and Methods* (Nos. 6-A55). U.S. Geological Survey. https://doi.org/10.3133/tm6A55

Langevin, C. D., Provost, A. M., Panday, S., & Hughes, J. D. (2022). Documentation for the MODFLOW 6 Groundwater Transport Model. In *Techniques and Methods* (Nos. 6-A61). U.S. Geological Survey. https://doi.org/10.3133/tm6A61

Lee, K. S. (2010). A Review on Concepts, Applications, and Models of Aquifer Thermal Energy Storage Systems. *Energies*, *3*(6), Article 6. https://doi.org/10.3390/en3061320

Ma, R., & Zheng, C. (2010). Effects of Density and Viscosity in Modeling Heat as a Groundwater Tracer. *Groundwater*, *48*(3), 380–389. https://doi.org/10.1111/j.1745-6584.2009.00660.x

Mahon, H., O'Connor, D., Friedrich, D., & Hughes, B. (2022). A review of thermal energy storage technologies for seasonal loops. *Energy*, *239*, 122207. https://doi.org/10.1016/j.energy.2021.122207

Park, J., Yang, G., Satija, A., Scheidt, C., & Caers, J. (2016). DGSA: A Matlab toolbox for distance-based generalized sensitivity analysis of geoscientific computer experiments. *Computers & Geosciences*, *97*, 15–29. https://doi.org/10.1016/j.cageo.2016.08.021

Perzan, Z., Babey, T., Caers, J., Bargar, J. R., & Maher, K. (2021). Local and Global Sensitivity Analysis of a Reactive Transport Model Simulating Floodplain Redox Cycling. *Water Resources Research*, *57*(12), e2021WR029723. https://doi.org/10.1029/2021WR029723

Pophillat, W., Attard, G., Bayer, P., Hecht-Méndez, J., & Blum, P. (2020). Analytical solutions for predicting thermal plumes of groundwater heat pump systems. *Renewable Energy*, *147*, 2696–2707. https://doi.org/10.1016/j.renene.2018.07.148

Possemiers, M., Huysmans, M., & Batelaan, O. (2014). Influence of Aquifer Thermal Energy Storage on groundwater quality: A review illustrated by seven case studies from Belgium. *Journal of Hydrology: Regional Studies*, *2*, 20–34. https://doi.org/10.1016/j.ejrh.2014.08.001

Scheidt, C., Li, L., & Caers, J. (2018). *Quantifying Uncertainty in Subsurface Systems*. John Wiley & Sons.

Sommer, W., Valstar, J., Leusbrock, I., Grotenhuis, T., & Rijnaarts, H. (2015). Optimization and spatial pattern of large-scale aquifer thermal energy storage. *Applied Energy*, *137*, 322–337. https://doi.org/10.1016/j.apenergy.2014.10.019

Stemmle, R., Arab, A., Bauer, S., Beyer, C., Blöcher, G., Bossennec, C., Dörnbrack, M., Hahn, F., Jaeger, P., Kranz, S., Mauerberger, A., Nordheim, J. N., Ohagen, M., Petrova, E., Regenspurg, S., Rettenmaier, D., Saadat, A., Sass, I., Scheytt, T., … Blum, P. (2025). Current research on aquifer thermal energy storage (ATES) in Germany. *Grundwasser*. https://doi.org/10.1007/s00767-025-00590-3

Stemmle, R., Hammer, V., Blum, P., & Menberg, K. (2022). Potential of low-temperature aquifer thermal energy storage (LT-ATES) in Germany. *Geothermal Energy*, *10*(1), 24. https://doi.org/10.1186/s40517-022-00234-2

Tas, L., Hartog, N., Bloemendal, M., Simpson, D., Robert, T., Thibaut, R., Zhang, L., & Hermans, T. (2025). Efficiency and heat transport processes of low-temperature aquifer thermal energy storage systems: New insights from global sensitivity analyses. *Geothermal Energy*, *13*(1), 2. https://doi.org/10.1186/s40517-024-00326-1

Tas, L., Simpson, D., & Hermans, T. (2023). Assessing the potential of low-transmissivity aquifers for aquifer thermal energy storage systems: A case study in Flanders (Belgium). *Hydrogeology Journal*, *31*(8), 2363–2380. https://doi.org/10.1007/s10040-023-02696-5

Vandersteen, K., & Gedeon, M. (2012). *Hydrogeology of North-East Belgium*.

Vandersteen, K., Gedeon, M., & Beerten, K. (2014). *A synthesis of hydraulic conductivity measurements of the subsurface in Northeastern Belgium.*

Visser, P. W., Kooi, H., & Stuyfzand, P. J. (2015). The thermal impact of aquifer thermal energy storage (ATES) systems: A case study in the Netherlands, combining monitoring and modeling. *Hydrogeology Journal*, *23*(3), 507–532. https://doi.org/10.1007/s10040-014-1224-z

VLAREM II. (2024). https://omgeving.vlaanderen.be/nl/vlarem

Winston, R. B. (2009). ModelMuse—A Graphical User Interface for MODFLOW-2005 and PHAST. In *Techniques and Methods* (Nos. 6-A29). U.S. Geological Survey. https://doi.org/10.3133/tm6A29

Zhang, Y., & Pinder, G. (2003). Latin hypercube lattice sample selection strategy for correlated random hydraulic conductivity fields. *Water Resources Research*, *39*(8). https://doi.org/10.1029/2002WR001822

Zuurbier, K. G., Zaadnoordijk, W. J., & Stuyfzand, P. J. (2014). How multiple partially penetrating wells improve the freshwater recovery of coastal aquifer storage and recovery (ASR) systems: A field and modeling study. *Journal of Hydrology*, *509*, 430–441. https://doi.org/10.1016/j.jhydrol.2013.11.057